CONDENSED MATTER PHYSICS

Real-time (nanoseconds) determination of liquid phase growth during shock-induced melting

Pritha Renganathan[1], Surinder M. Sharma[1]†, Stefan J. Turneaure[1], Yogendra M. Gupta[1,2]*

Melting of solids is a fundamental natural phenomenon whose pressure dependence has been of interest for nearly a century. However, the temporal evolution of the molten phase under pressure has eluded measurements because of experimental challenges. By using the shock front as a fiducial, we investigated the time-dependent growth of the molten phase in shock-compressed germanium. In situ x-ray diffraction measurements at different times (1 to 6 nanoseconds) behind the shock front quantified the real-time growth of the liquid phase at several peak stresses. These results show that the characteristic time for melting in shock-compressed germanium decreases from ~7.2 nanoseconds at 35 gigapascals to less than 1 nanosecond at 42 gigapascals. Our melting kinetics results suggest the need to consider heterogeneous nucleation as a mechanism for shock-induced melting and provide an approach to measuring melting kinetics in shock-compressed solids.

INTRODUCTION

Melting of solids constitutes a ubiquitous structural change commonly encountered in everyday life. Pressure effects on melting have been studied extensively since Bridgman's pioneering work (1, 2), and pressure (P)–temperature (T) phase diagrams serve as a starting point for understanding different states of matter in a wide range of scientific disciplines (3–13). Despite the vast body of literature related to pressure effects on the melting transition, experimental determination of the melting kinetics or the growth of the liquid state, particularly on short time scales (nanoseconds to microseconds), remains an outstanding challenge.

The use of shock wave compression to achieve melting at high pressures is well established (14); the propagating shock front imparts a near-discontinuous change in temperature and pressure to the pristine solid ahead of the shock wave. Sound speed measurements in the shock-compressed state are commonly used to determine the onset of melting in shock experiments (15–19). Although these measurements along with the Hugoniot data are useful for developing equations of state (EOS) at high pressures, they do not provide details of the mixed phase composition—determination of liquid and solid phase fractions.

Recent developments regarding real-time, in situ x-ray diffraction (XRD) measurements in shock-compressed solids constitute a paradigm shift in understanding shock-induced structural transformations (20–26). In situ observations of the coexistence of crystalline and liquid phases in shock-compressed iron (27) demonstrated the first-order character of shock-induced melting. However, the lack of time-resolved measurements precluded observations of the liquid phase growth and the determination of melting kinetics. We report here on an innovative approach to achieve in situ XRD measurements at different times behind the shock front, resulting in time-resolved determination of the mixed phase composition. Our results on shock-compressed germanium reveal

melting kinetics that are notably more rapid than current theoretical predictions and make the case for heterogeneous nucleation as a mechanism to understand shock-induced melting.

[100] Ge single crystals were chosen to examine the temporal growth of the liquid phase, for this first study, because of the following factors: high-pressure and high-temperature Ge data under static compression (28–30); continuum measurements on shock-compressed Ge single crystals (31); and recent XRD measurements on thin [100] Ge crystals in plate impact shock experiments (32). The plate impact XRD measurements, obtained more than 150 ns behind the shock front, demonstrated a fully liquid state at and above 35 GPa. In contrast to the plate impact experiments, the XRD measurements presented here provide the temporal evolution of the shock-induced liquid state at shorter times. Although the loading history and measurement times are different in the plate impact and laser shock experiments, other experimental variables (peak stresses, sample thickness, and the x-ray source) are similar for the two types of shock experiments.

RESULTS

Using the configuration shown in Fig. 1A, XRD and wave profile measurements were obtained in laser shock experiments (33) conducted at the Dynamic Compression Sector, located at the Advanced Photon Source. Targets consisting of a 50 μm-thick Kapton ablator bonded to thin (~33 μm) [100] Ge crystals were ablated generating a shock wave into the sample. For the two types of targets used in our experiments (with or without LiF window), the particle velocity histories were recorded at the sample rear surface using laser interferometry (34) and representative profiles are shown in Fig. 1B. Shock wave amplitudes were determined precisely by analyzing these wave profiles and the calculated stresses demonstrated good consistency between the two types of targets (35).

Figure 2 shows representative single-pulse (~100 ps duration) XRD patterns, obtained using ~23.6 keV x-rays, for [100] Ge laser-shocked between 24.2 and 46.5 GPa. Although the overall XRD measurement approach is similar to that used in previous laser shock experiments (24, 27, 36), the present work incorporated

[1]Institute for Shock Physics, Washington State University, Pullman, WA 99164, USA. [2]Department of Physics and Astronomy, Washington State University, Pullman, WA 99164, USA.
*Corresponding author. Email: ymgupta@wsu.edu
†Present address: Physics Group, Bhabha Atomic Research Centre, Mumbai 400085, India.
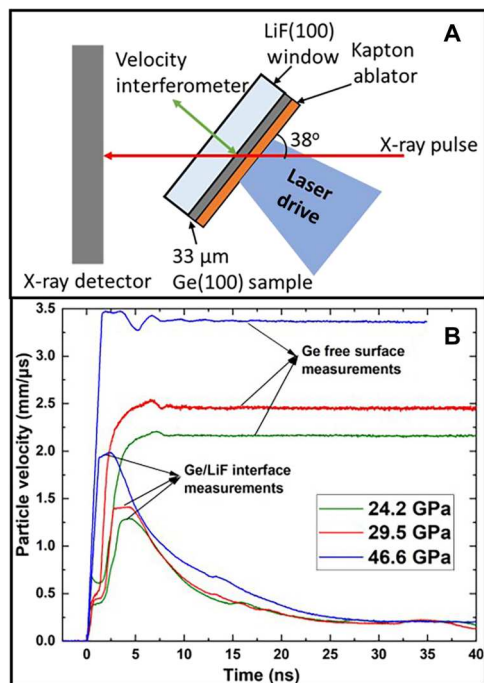
Fig. 1. Experimental setup and results. (**A**) Experimental configuration used for in situ XRD and wave profile measurements in laser-shocked Ge. (**B**) Representative particle velocity histories measured in the present work.

a key noteworthy feature, obtaining XRD measurements at different times (ranging from 1 to 6 ns) after the shock wave entered the Ge sample. XRD data at different times, for the same peak stress, are necessary to reliably obtain the temporal evolution of the liquid phase. Since the XRD measurements are made through the entire sample thickness, both the shocked and unshocked regions contribute to the data. Hence, the single-crystal diffraction spots, corresponding to the unshocked Ge, were masked before analyzing the XRD data.

The lineouts below each XRD pattern correspond to the one-dimensional line profile (intensity versus scattering angle) obtained by integrating the recorded XRD images azimuthally using Fit2D (37, 38). At 24.2 and 29.5 GPa, we observe non-uniform diffraction rings representing the textured high-pressure solid Ge phase. Between 34.8 and 42.4 GPa, we observe (i) the emergence of a smooth broad diffraction ring, and (ii) the gradual disappearance of the second diffraction peak (corresponding to crystalline Ge) with increasing stress.

Figure 3A shows excellent agreement between the simulated line profiles and the measured line profiles for the representative results shown in Fig. 2. The simulated line profiles incorporated the target information, the spectral flux, and x-ray absorption in the target; details regarding the simulations are presented in sections S2 and S4 in the Supplementary Materials (35). The diffraction profiles at 24.2 and 29.5 GPa correspond to the β-Sn structure, also observed in the plate impact experiments (32). Measured line profiles in laser shock and plate impact experiments (32) at these stresses (fig. S5) (35) show good agreement, demonstrating that the cd to β-Sn phase transformation is very rapid and does not depend on the peak state duration. The a and c lattice parameters for laser-shocked Ge were determined by fitting the first two doublet peaks

in the high-pressure β-Sn structure since these peaks are sharp and clearly discernable. Within experimental scatter, these lattice parameters show good consistency with previous plate impact results (see fig. S8) (35).

Notable comments are in order regarding the XRD simulations between 34.8 and 42.4 GPa. To obtain a good fit to the measured line profiles using only the solid phase (β-Sn), a large increase in the amount of line broadening was essential (see fig. S7A) (35). This phenomenon is similar to the results observed for laser-shocked Fe (27) and suggests that the line broadening increase is due to partial melting of the shocked Ge—a consequence of the superposition of the broad liquid diffraction ring on the first two β-Sn doublets. To determine the lattice parameters of the β-Sn structure and to estimate the liquid fraction in the mixed phase region, we used the procedure described previously (27). Using that procedure, the measured line profiles were fit to a superposition of simulated crystalline β-Sn diffraction peaks and a shifted liquid line profile from the 46.5 GPa experiment, representing the fully molten Ge phase. The liquid line profile fraction resulting in the best overall fit (corrected for unshocked Ge in the experiment) provided the determination of the liquid fraction. The calculated liquid percentage as a function of peak stress in shock-compressed Ge is shown in Fig. 3B. The uncertainty in determining the liquid volume fraction using this approach is expected to be ~8 to 10% (see section S4) (35).

Figure 4 shows the growth of the liquid phase as a function of time for three peak stresses: nominally 35, 38, and 42 GPa. The dashed lines shown in Fig. 4 correspond to a fit based on the phenomenological Johnson-Mehl-Avrami-Kolmogorov (JMAK) equation (39–44), widely used to describe phase transformation kinetics

$$x(t) = 1 - \exp\left[-\left(\frac{t}{\tau}\right)^{m}\right] \quad (1)$$

where $x(t)$ is volume fraction of the emergent phase (in this case, liquid volume fraction) at time t, τ is the time constant of phase growth, and m corresponds to different geometries of the liquid phase: spherical (three dimensions, $m = 3$), disk-shaped (two dimensions, $m = 2$), and rod-shaped (one dimension, $m = 1$). Since different regions in the shock-compressed sample experience different peak stress durations, depending on their distance from the shock front, care is needed in evaluating the liquid phase fraction using the JMAK equation as explained below.

The shock-compressed sample thickness, denoted as λ, can be considered as a large collection of thin zones—each having a thickness dz, where z (bounded by 0 and λ) denotes the distance behind the shock front along the shock propagation direction. Thus, the liquid phase fraction at any location, z, can be written as

$$x(z, t) = 1 - \exp\left[-\left(\left\{\frac{z}{\lambda}\right\}\frac{t}{\tau}\right)^{m}\right] \quad (2)$$

and the liquid phase fraction for the entire shock-compressed sample is given by

$$x(t) = \frac{1}{\lambda}\int_{0}^{\lambda} x(z, t)dz \quad (3)$$

Initial fits to the data gave m as ~1.5 for 34.9 GPa and ~0.7 for 38.2 GPa, qualitatively suggesting a one-dimensional (needle like) growth. With $m = 1$ (a reasonable approximation), the fits to our
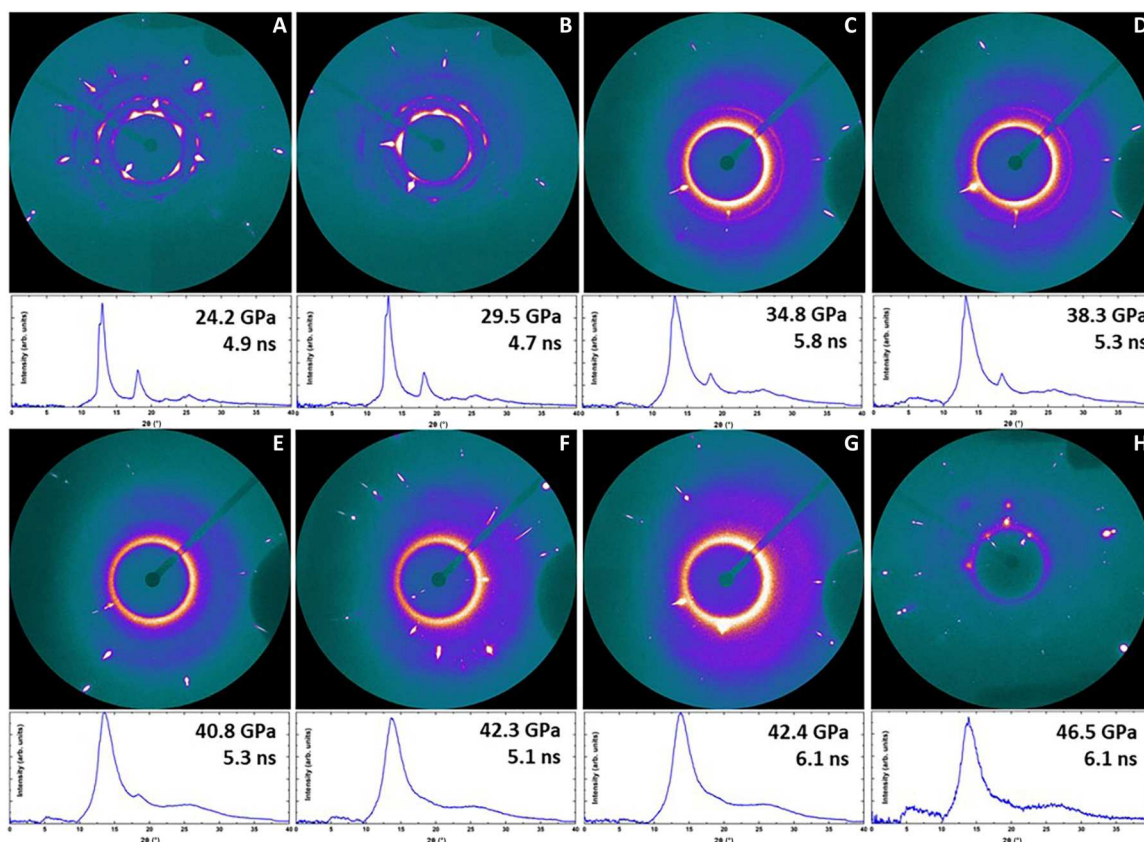
Fig. 2. Representative single-pulse XRD patterns and corresponding lineouts. (A-H) Single-pulse XRD patterns obtained after shock enters the sample; the peak stress and XRD measurement time for each experiment are shown in the lineouts. Bright localized spots in the XRD patterns are from unshocked Ge single-crystal samples.

data resulted in: τ = 7.2, 2.0, and 0.3 ns for the experiments at 34.9, 38.2, and 42.3 GPa, respectively.

Figure 4 provides several interesting insights regarding the melting transition kinetics in shock-compressed Ge: (i) Beyond a threshold stress, the molten phase abundance increases rapidly and is quantifiable within ~35 to 42 GPa; (ii) increase in the peak stress substantially shortens the time needed for the same fractional abundance (~95%) of the liquid phase: ~144 ns at 35 GPa, ~40 ns at 38 GPa, and ~6.6 ns at 42 GPa; and (iii) beyond 42 GPa, the temporal evolution of the liquid phase would likely be too rapid to measure in our experiments, implying almost instantaneous (sub-nanosecond) melting. We note that the previous observation of complete melting of shocked Ge at ~35 GPa in plate impact experiments (32) is consistent with the results in Fig. 4, since the earlier XRD measurements (32) were made at longer times (>150 ns) behind the shock front than the times shown in Fig. 4. However, because of loading history differences in the two sets of shock experiments, care needs to be exercised in making comparisons.

DISCUSSION

Both laser shock and plate impact (32) experiments have established 35 GPa as the melting threshold along the Ge Hugoniot. However, the lack of temperature measurements in shocked Ge requires the use of a theoretical approach to estimating temperatures along the Hugoniot. The theoretical multiphase EOS developed by Crockett

et al. (45) shows that the Ge Hugoniot crosses the P-T melt boundary, determined from static compression studies (46–51), at ~50 GPa. In view of the XRD results, the multiphase Ge EOS will need to be revised.

To estimate shock temperatures, we used the following ad hoc approach—shifting the Hugoniot from (45) to cross the statically determined melt boundary at 35 GPa (see fig. S9) and using the shifted Hugoniot to estimate the shock temperatures. The resulting temperatures are 1354 K at 35 GPa and 1534 K at 38 GPa. We note that the melt boundary determined from static P-T measurements provides a temperature of 1410 K at 38 GPa. Because of the closeness of these temperatures (within 10%), temperatures from the shifted Hugoniot are used in the following discussion.

To gain mechanistic insight into the rapid melting kinetics observed in this work, we first note some findings obtained from experimental studies and molecular dynamics (MD) simulations related to melting. Experiments at ambient conditions show that melting begins at free surfaces and grain boundaries and then propagates (52). To approximate the growth velocity of the molten phase due to homogeneous melting for our work, we consider the propagation of melting from an interface. For a ~33 μm thick Ge single crystal, if we assume instantaneous melting at the shocked surface, then the melting of the entire crystal in ~4τ (corresponding to ~75% melting) would require a solid-liquid interface velocity to be greater than 1100 m/s at 35 GPa and greater than 4000 m/s at 38 GPa. However, most of the MD simulations indicate that the melt
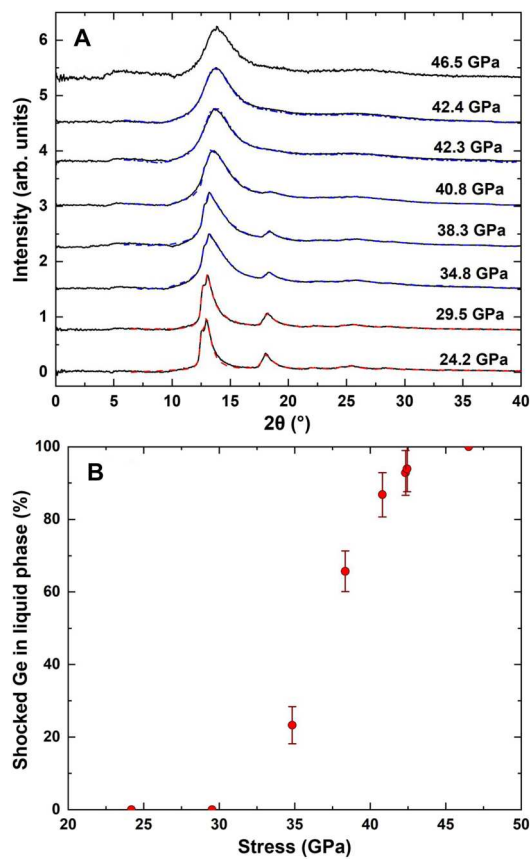
Fig. 3. Shocked Ge XRD results. (**A**) Comparison of measured and simulated Ge XRD lineouts. Solid lines are the measured line profiles shown in Fig. 2, while red and blue dashed lines correspond to the best fit simulations. Red dashed lines are from simulations incorporating only the β-Sn crystalline diffraction peaks. Blue dashed lines are from simulations that incorporated a superposition of the crystalline diffraction peaks and the broad liquid scattering line profile. Experiments at 42.3 and 42.4 GPa correspond to at least 95% liquid, suggesting that shocked Ge completely melts beyond 42.4 GPa. (**B**) Percentage of the shocked Ge in the liquid phase with increasing peak stress for the XRD data shown in Fig. 2. The red symbols were obtained by fitting the measured line profiles to a superposition of the simulated crystalline β-Sn diffraction peaks and the liquid line profile.

interface velocity for ~20% superheating (beyond the melting temperature) is a few hundred meters per second (~450 m/s in copper) (*53*). Similar simulations of heterogeneous melting initiated at the grain boundaries give comparable velocity of 450 m/s in Ni at 20% superheating (*54*) and 550 m/s in Al at comparable superheating (*55*). Phenomenological modeling of melting in Al suggests that, at a given reduced temperature (T/T_m, T_m being the melting temperature at a pressure), the growth rate of the molten phase is not very sensitive to the pressure (*56*).

In view of the above comments, a reasonable explanation of our observed results in terms of presently known melting models would require an extreme level of superheating. On the basis of the temperature estimates noted above for shocked Ge (fig. S9), extreme superheating is not a plausible explanation, and an alternate melting mechanism needs to be considered under shock compression.

Our experimental geometry suggests that, under shock compression, melting is likely nucleated at the shock front. Uniaxial strain
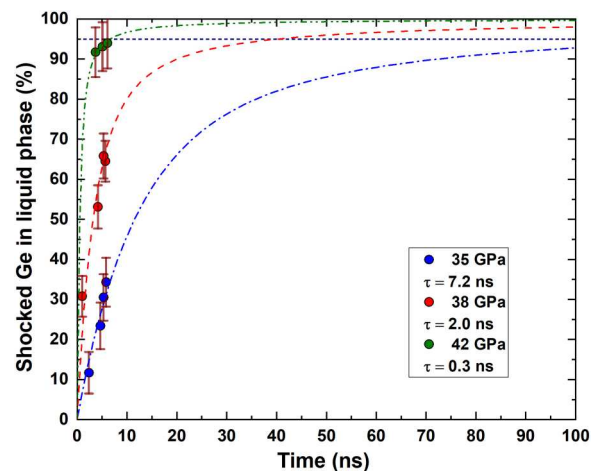

Fig. 4. Ge liquid volume fraction as a function of time for different peak stresses. The dashed lines correspond to a fit based on the phenomenological JMAK equation (*39–44*) The time required for the same fractional abundance (~95%) of the liquid phase is shown by the purple horizontal dashed line; the ~95% line intersects the 35 GPa curve at 144 ns. Uncertainty in the liquid volume fraction is estimated to be 8 to 10%.

compression and the cubic diamond (cd) to β-Sn phase change will convert the Ge single crystal into a heterogeneous state for the nucleation of melting. For a shock speed of 5.06 km/s (*31*), the trailing heterogeneous melting, which also does not require much superheating (*57*), would explain the observed results if the grain sizes are small and melting nucleation takes place widely at these grains. For example, assuming that the melting growth velocity is only a few hundred meters per second, as suggested by MD simulations noted above, then the observed rapidity of melting implies that the grain size for heterogeneous melting may be a few hundred nanometers. Although we cannot confirm the size of the grains in the present work, the following observations are consistent with this suggestion. Several in situ experiments on phase transitions in materials suggest that the size of coherent diffracting volume of the emergent phase is of the order of tens of nanometers (*20*, *36*, *58*). In addition, although qualitative in nature, $m \approx 1$ in Eq. 1 suggests needle-like growth of the molten phase. Such a small size of grains and needle-like growth are qualitatively consistent with the hypothesis that melting is facilitated by dislocations (*59–61*). However, we emphasize that these qualitative arguments need to be validated by more detailed theoretical investigations. These calculations may also help determine the preferred nucleation sites for melting and a mechanism for the growth of the molten phase in the shock-compressed solids.

By combining well-defined, reproducible laser shock experiments with synchrotron-based XRD measurements, the real-time response of shock-compressed [100] Ge was examined to 46 GPa. High-quality XRD results were obtained in the high-pressure (β-Sn) solid phase (below 35 GPa), in the mixed or β-Sn/liquid phase (35 to 42 GPa), and upon complete melting (beyond 42 GPa). Using XRD measurements at different times (ranging from 1 to 6 ns) behind the shock front, we provide the first experimental determination of the real-time growth of the liquid phase. The melting kinetics data obtained at three different peak stresses could be fitted using the phenomenological JMAK equation (widely used to model phase

transformation kinetics) resulting in the following melting characteristic times: 7.2 ns at 35 GPa, 2.0 ns at 38 GPa, and 0.3 ns at 42 GPa.

The experimental results presented here demonstrate the need to incorporate melting kinetics into multiphase EOS descriptions for use in shock compression studies and the need for detailed theoretical investigations to achieve a mechanistic understanding of the observed rapid melting kinetics. Finally, we note that the experimental developments presented here for Ge provide an approach for measuring melting kinetics in other shock-compressed solids.

MATERIALS AND METHODS

All the samples used in this study were cut from high-quality (99.99% pure) Ge single-crystal boules, oriented to within 1° of the [100] direction. The cut surfaces were ground flat and then hand-polished to ~33 μm in thickness, using diamond suspension having particles down to 1 μm in size. The Ge samples were characterized when the sample thickness was ~1 mm. The average density, measured using the Archimedean method, was 5.328 ± 0.002 g/cm^3. Using the pulse-echo technique, the average longitudinal and shear sound speeds were measured to be 4.97 ± 0.03 and 3.56 ± 0.02 mm/μs, respectively. These values are in excellent agreement with values reported in the literature (31).

The experimental configuration used in this work is shown in Fig. 1A. The targets consisted of a 50-μm-thick Kapton ablator bonded to thin (~33 ± 4 μm) [100] Ge crystals. Two types of targets were used as follows: (i) Some targets used approximately 1-mm-thick LiF windows to obtain interface particle velocity profiles to calculate the peak stress and (ii) other targets only had free surfaces (no LiF) to obtain optimal XRD data and free surface velocity measurements. The target was ablated using a 500-μm-diameter drive pulse generating a 10-ns duration shock wave into the sample (33). Laser ablation of the Kapton layer results in a shock wave propagating through the Ge sample. A velocity interferometer system for any reflector (34) was used to record the velocity histories at the rear surface of the Ge sample (Fig. 1B). Peak stress in the Ge sample was obtained by analyzing the measured wave profiles (section S3) (35). The peak stresses in the present work ranged from ~24 to 46 GPa.

The XRD measurements and analysis are described in detail in the Supplementary Materials (35), and only a brief overview is presented here. The overall XRD measurement approach is similar to that used in previous studies (24, 27, 36). The in situ XRD measurements were obtained using the x-ray pulse (100-ps duration) from the Advanced Photon Source hybrid mode. By appropriately synchronizing the x-ray pulse and the laser drive pulse, XRD measurements were obtained over a range of times (1 to 6 ns) after the shock wave entered the sample. Since the XRD measurements are made through the entire sample thickness, these data include contributions from the unshocked and shocked Ge, and the unshocked diffraction spots were masked before analyzing the XRD data (35).

Supplementary Materials

This PDF file includes:
Sections S1 to S5
Figs. S1 to S10
Table S1
References

REFERENCES AND NOTES

1. P. W. Bridgman, The phase diagram of water to 45,000 kg/cm^2. *J. Chem. Phys.* **5**, 964–966 (1937).
2. P. W. Bridgman, *The Physics of High Pressure* (G. Bell and Sons, 1952).
3. D. A. Young, *Phase Diagrams of the Elements* (Univ. of California Press, 1991).
4. R. Boehler, Temperatures in the Earth's core from melting-point measurements of iron at high static pressures. *Nature* **363**, 534–536 (1993).
5. D. Alfe, M. J. Gillan, G. D. Price, The melting curve of iron at the pressures of the Earth's core from ab initio calculations. *Nature* **401**, 462–464 (1999).
6. F. Datchi, P. Loubeyre, R. LeToullec, Extended and accurate determination of the melting curves of argon, helium, ice (H$_2$O), and hydrogen (H$_2$). *Phys. Rev. B* **61**, 6535–6546 (2000).
7. D. Alfè, L. Vočadlo, G. D. Price, M. J. Gillan, Melting curve of materials: Theory versus experiments. *J. Phys. Condens. Matter* **16**, S973–S982 (2004).
8. C. L. Guillaume, E. Gregoryanz, O. Degtyareva, M. I. McMahon, M. Hanfland, S. Evans, M. Guthrie, S. V. Sinogeikin, H.-K. Mao, Cold melting and solid structures of dense lithium. *Nat. Phys.* **7**, 211–214 (2011).
9. D. Andrault, S. Petitgirard, G. l. Nigro, J.-L. Devidal, G. Veronesi, G. Garbarino, M. Mezouar, Solid-liquid iron partitioning in Earth's deep mantle. *Nature* **487**, 354–357 (2012).
10. P. A. Bland, G. S. Collins, T. M. Davison, N. M. Abreu, F. J. Ciesla, A. R. Muxworthy, J. Moore, Pressure-temperature evolution of primordial solar system solids during impact-induced compaction. *Nat. Commun.* **5**, 5451 (2014).
11. R. N. Widmer, G. I. Lampronti, S. Anzellini, R. Gaillac, S. Farsang, C. Zhou, A. M. Belenguer, C. W. Wilson, H. Palmer, A. K. Kleppe, M. T. Wharmby, X. Yu, S. M. Cohen, S. G. Telfer, S. A. T. Redfern, F. X. Coudert, S. G. MacLeod, T. D. Bennett, Pressure promoted low-temperature melting of metal–organic frameworks. *Nat. Mater.* **18**, 370–376 (2019).
12. R. Sinmyo, K. Hirose, Y. Ohishi, Melting curve of iron to 290 GPa determined in a resistance-heated diamond-anvil cell. *Earth Planet. Sci. Lett.* **510**, 45–52 (2019).
13. S. Tagawa, G. Helffrich, K. Hirose, Y. Ohishi, High-pressure melting curve of FeH: Implications for eutectic melting between Fe and non-magnetic FeH. *J. Geophys. Res. Solid Earth* **127**, e2022JB024365 (2022).
14. G. E. Duvall, R. A. Graham, Phase transitions under shock-wave loading. *Rev. Mod. Phys.* **49**, 523–579 (1977).
15. J. M. Brown, R. G. McQueen, Phase transitions, Grüneisen parameter, and elasticity for shocked iron between 77 GPa and 400 GPa. *J. Geophys. Res. Solid Earth* **91**, 7485–7494 (1986).
16. J. H. Nguyen, N. C. Holmes, Melting of iron at the physical conditions of the Earth's core. *Nature* **427**, 339–342 (2004).
17. B. J. Jensen, F. J. Cherne, J. C. Cooley, M. V. Zhernokletov, A. E. Kovalev, Shock melting of cerium. *Phys. Rev. B* **81**, 214109 (2010).
18. P. Renganathan, T. S. Duffy, Y. M. Gupta, Sound velocities in shock-compressed soda lime glass: Melting and liquid-state response. *Phys. Rev. B* **104**, 014113 (2021).
19. M. K. Wallace, J. M. Winey, Y. M. Gupta, Sound speed measurements in silver shock compressed to 300 GPa: Solid-state transition, melting, and liquid-state response. *Phys. Rev. B* **104**, 214106 (2021).
20. S. J. Turneaure, N. Sinclair, Y. M. Gupta, Real-time examination of atomistic mechanisms during shock-induced structural transformation in silicon. *Phys. Rev. Lett.* **117**, 045502 (2016).
21. R. Briggs, M. G. Gorman, A. L. Coleman, R. S. McWilliams, E. E. McBride, D. McGonegle, J. S. Wark, L. Peacock, S. Rothman, S. G. Macleod, C. A. Bolme, A. E. Gleason, G. W. Collins, J. H. Eggert, D. E. Fratanduono, R. F. Smith, E. Galtier, E. Granados, H. J. Lee, B. Nagler, I. Nam, Z. Xing, M. I. McMahon, Ultrafast x-ray diffraction studies of the phase transitions and equation of state of scandium shock compressed to 82 GPa. *Phys. Rev. Lett.* **118**, 025501 (2017).
22. S. J. Tracy, S. J. Turneaure, T. S. Duffy, In situ x-ray diffraction of shock-compressed fused silica. *Phys. Rev. Lett.* **120**, 135702 (2018).
23. A. L. Coleman, M. G. Gorman, R. Briggs, R. S. McWilliams, D. McGonegle, C. A. Bolme, A. E. Gleason, D. E. Fratanduono, R. F. Smith, E. Galtier, H. J. Lee, B. Nagler, E. Granados, G. W. Collins, J. H. Eggert, J. S. Wark, M. I. McMahon, Identification of phase transitions and metastability in dynamically compressed antimony using ultrafast x-ray diffraction. *Phys. Rev. Lett.* **122**, 255704 (2019).
24. S. M. Sharma, S. J. Turneaure, J. M. Winey, Y. M. Gupta, What determines the fcc-bcc structural transformation in shock compressed noble metals? *Phys. Rev. Lett.* **124**, 235701 (2020).
25. T. Okuchi, Y. Seto, N. Tomioka, T. Matsuoka, B. Albertazzi, N. J. Hartley, Y. Inubushi, K. Katagiri, R. Kodama, T. A. Pikuz, N. Purevjav, K. Miyanishi, T. Sato, T. Sekine, K. Sueda, K. A. Tanaka, Y. Tange, T. Togashi, Y. Umeda, T. Yabuuchi, M. Yabashi, N. Ozaki, Ultrafast olivine-ringwoodite transformation during shock compression. *Nat. Commun.* **12**, 4305 (2021).

26. M. T. Beason, B. J. Jensen, Examination of the cerium α-ε phase transition under dynamic loading with x-ray diffraction. *Phys. Rev. B* **105**, 214107 (2022).

27. S. J. Turneaure, S. M. Sharma, Y. M. Gupta, Crystal structure and melting of Fe shock compressed to 273 GPa: In situ x-ray diffraction. *Phys. Rev. Lett.* **125**, 215702 (2020).

28. J. C. Jamieson, Crystal structures at high pressures of metallic modifications of silicon and germanium. *Science* **139**, 762–764 (1963).

29. A. Mujica, A. Rubio, A. Muñoz, R. J. Needs, High-pressure phases of group-IV, III-V, and II-VI compounds. *Rev. Mod. Phys.* **75**, 863–912 (2003).

30. X.-J. Chen, C. Zhang, Y. Meng, R.-Q. Zhang, H.-Q. Lin, V. V. Struzhkin, H.-K. Mao, β—Tin→Imma→sh phase transitions of germanium. *Phys. Rev. Lett.* **106**, 135502 (2011).

31. W. H. Gust, E. B. Royce, Axial yield strengths and phase-transition stresses for ⟨100⟩, ⟨110⟩, and ⟨111⟩ germanium. *J. Appl. Phys.* **43**, 4437–4442 (1972).

32. P. Renganathan, S. J. Turneaure, S. M. Sharma, Y. M. Gupta, Structural transformations including melting and recrystallization during shock compression and release of germanium up to 45 GPa. *Phys. Rev. B* **99**, 134101 (2019).

33. X. Wang, P. Rigg, J. Sethian, N. Sinclair, N. Weir, B. Williams, J. Zhang, J. Hawreliak, Y. Toyoda, Y. Gupta, Y. Li, D. Broege, J. Bromage, R. Earley, D. Guy, J. Zuegel, The laser shock station in the dynamic compression sector. I. *Rev. Sci. Instrum.* **90**, 053901 (2019).

34. L. M. Barker, R. E. Hollenbach, Laser interferometer for measuring high velocities of any reflecting surface. *J. Appl. Phys.* **43**, 4669–4675 (1972).

35. "See the Supplementary Materials for additional experimental details and results and methods used for analyzing the diffraction simulations and results."

36. S. M. Sharma, S. J. Turneaure, J. M. Winey, Y. Li, P. Rigg, A. Schuman, N. Sinclair, Y. Toyoda, X. Wang, N. Weir, J. Zhang, Y. M. Gupta, Structural transformation and melting in gold shock compressed to 355 GPa. *Phys. Rev. Lett.* **123**, 045702 (2019).

37. A. P. Hammersley, "FIT2D: An introduction and overview" (ESRF Internal Report ESRF97HA02T, ESRF, 1997).

38. A. P. Hammersley, S. O. Svensson, M. Hanfland, A. N. Fitch, D. Hausermann, Two-dimensional detector software: From real detector to idealised image or two-theta scan. *High Press Res.* **14**, 235–248 (1996).

39. A. N. Kolmogorov, On the statistical theory of the crystallization of metals. *Bull. Acad. Sci. USSR, Math. Ser.* **1**, 355–359 (1937).

40. W. A. Johnson, R. F. Mehl, Reaction kinetics in processes of nucleation and growth. *Trans. Am. Inst. Min. Metall. Pet. Eng.* **135**, 416–442 (1939).

41. M. Avrami, Kinetics of phase change. I General theory. *J. Chem. Phys.* **7**, 1103–1112 (1939).

42. M. Avrami, Kinetics of phase change. II Transformation-time relations for random distribution of nuclei. *J. Chem. Phys.* **8**, 212–224 (1940).

43. M. Avrami, Granulation, phase change, and microstructure kinetics of phase change. III. *J. Chem. Phys.* **9**, 177–184 (1941).

44. J. W. Christian, *The Theory of Transformations in Metals and Alloys* (Pergamon, 1975), vol. 15.

45. S. D. Crockett, G. de Lorenzi-Venneri, J. D. Kress, S. P. Rudin, Germanium multiphase equation of state, in *Journal of Physics: Conference Series 500* (Institute of Physics Publishing, 2014), vol. 500, p. 032006.

46. L. C. Kelsall, M. Peña-Alvarez, M. Martinez-Canales, J. Binns, C. J. Pickard, P. Dalladay-Simpson, R. T. Howie, E. Gregoryanz, High-temperature phase transitions in dense germanium. *J. Chem. Phys.* **154**, 174702 (2021).

47. V. B. Prakapenka, A. Kubo, A. Kuznetsov, A. Laskin, O. Shkurikhin, P. Dera, M. L. Rivers, S. R. Sutton, Advanced flat top laser heating system for high pressure research at GSECARS: Application to the melting behavior of germanium. *High Press Res.* **28**, 225–235 (2008).

48. S. Pasternak, G. Aquilanti, S. Pascarelli, R. Poloni, B. Canny, M. V. Coulet, L. Zhang, A diamond anvil cell with resistive heating for high pressure and high temperature x-ray diffraction and absorption studies. *Rev. Sci. Instrum.* **79**, 085103 (2008).

49. F. P. Bundy, Phase diagrams of silicon and germanium to 200 kbar, 1000°c. *J. Chem. Phys.* **41**, 3809–3814 (1964).

50. A. Jayaram, W. Klement Jr., G. C. Kennedy, Melting and polymorphism at high pressures in some group IV elements and III—V compounds with the diamond/zincblende structure. *Phys. Rev.* **130**, 540–547 (1963).

51. J. F. Cannon, Behavior of the elements at high pressures. *J. Phys. Chem. Ref. Data Monogr.* **3**, 781–824 (1974).

52. N. G. Ainslie, J. D. Mackenzie, D. Turnbull, Melting kinetics of quartz and cristobalite. *J. Phys. Chem.* **65**, 1718–1724 (1961).

53. V. I. Mazhukin, A. V. Shapranov, V. E. Perezhigin, O. N. Koroleva, A. V. Mazhukin, Kinetic melting and crystallization stages of strongly superheated and supercooled metals. *Math. Models Comput. Simul.* **9**, 448–456 (2017).

54. D. S. Ivanov, L. V. Zhigilei, Kinetic limit of heterogeneous melting in metals. *Phys. Rev. Lett.* **98**, 195701 (2007).

55. Y. Liao, M. Xiang, X. Zhu, J. Chen, X. Tian, L. Ge, Heterogeneous melting kinetics in polycrystalline aluminum. *PLOS ONE* **15**, e0230028 (2020).

56. M. Xiang, S. Jiang, J. Chen, Theoretical investigations on melting/crystallization kinetics in overheated/overcooled aluminum at high pressures. *J. Appl. Phys.* **126**, 125113 (2019).

57. M. Xiang, Y. Liao, G. Li, J. Chen, Coupling of homogeneous and heterogeneous melting kinetics in overheated polycrystalline materials. *Comput. Mater. Sci.* **173**, 109421 (2020).

58. S. J. Turneaure, Y. M. Gupta, Micro-strains, local stresses, and coherently diffracting domain size in shock compressed Al(100) single crystals. *J. Appl. Phys.* **131**, 225902 (2022).

59. D. Kuhlmann-Wilsdorf, Theory of melting. *Phys. Rev.* **140**, A1599 (1965).

60. R. M. J. Cotterill, The physics of melting. *J. Cryst. Growth* **48**, 582–588 (1980).

61. L. Burakovsky, D. L. Preston, Analysis of dislocation mechanism for melting of elements. *Solid State Commun.* **115**, 341–345 (2000).

62. J. M. Walsh, R. H. Christian, Equation of state of metals from shock wave measurements. *Phys. Rev.* **97**, 1544–1556 (1955).

63. P. A. Rigg, M. D. Knudson, R. J. Scharff, R. S. Hixson, Determining the refractive index of shocked [100] lithium fluoride to the limit of transmissibility. *J. Appl. Phys.* **116**, 033515 (2014).